Marine Heatwaves Disrupt Phytoplankton Communities Through Trait-dependent Selection

Hyo-Jeong Kim[1], Stephanie Dutkiewicz[2], Junwoo Lee[1], Ibrahim Hoteit[3], Yixin Wang[3], Soon-Il An[1], Oliver Jahn[2], and Hajoon Song[1,*]

[1]Yonsei University, Seoul, South Korea. E-mail: kimhj29@yonsei.ac.kr
[2]Massachusetts Institute of Technology, Cambridge, USA
[3]King Abdullah University of Science and Technology, Thuwal, Saudi Arabia

* Corresponding Author: Hajoon Song (hajsong@yonsei.ac.kr)

Abstract

Phytoplankton communities, key regulators of marine ecosystems and the global carbon cycle, are susceptible to sea surface temperature variability, such as marine heatwaves (MHWs). However, their trait-dependent responses and the resulting compositional shifts during MHWs remain poorly understood. Here, using an advanced global ocean–biogeochemical model that resolves 310 phytoplankton trait types, we show that MHWs act as trait-selective disturbances. Decreases in biomass during MHWs, particularly in the equatorial Pacific and Indian Ocean, are generally accompanied by significant diversity loss and an enhanced dominance of small, warm-preferring types. However, short and strong heatwaves in the Pacific can promote elevated diversity. These contrasting patterns are shaped by the interplay between heatwave characteristics and background environmental conditions. Such restructuring in phytoplankton communities may have cascading effects on the food web and the biological carbon pump, highlighting the need to account for diverse traits when assessing climatic impacts on phytoplankton communities.

Introduction

Phytoplankton are the base of the marine food web and key players in the carbon cycle, exhibiting a wide range of morphological (e.g., cell size), genetic, physiological, and ecological traits[1,2]. Their spatiotemporal distributions are shaped by multiple factors, including seasonal cycles, transport, stochastic disturbances, and environmental/trophic selection[3]. Climate forcings, such as El Niño–Southern Oscillation (ENSO) and extreme events, such as marine heatwaves (MHWs)[4–6], can modulate phytoplankton communities through their influence on oceanic transport and environmental fitness[4–6]. Importantly, vulnerability and adaptability to such climate stressors can be trait-dependent, varying among phytoplankton with distinct thermal and nutrient preferences. The resulting shifts in community composition due to stressors can cause socio-ecological consequences through impacts on higher trophic levels[7–10]. Nevertheless, trait-dependent responses of phytoplankton to climate forcing remain relatively understudied, primarily due to a lack of reliable, continuous observations with sufficient taxonomic coverage[11].

Models can provide a useful framework to address this challenge. For instance, previous model-based studies identified that mean phytoplankton diversity distributions are collectively shaped by competition for multiple nutrients, grazing pressure, sinking velocity, and transport by ocean currents[12–16]. Yet, a large knowledge gap remains regarding whether ecosystem responses to transient climate extremes follow principles inferred from long-term mean state or involve distinct mechanisms. Unraveling this uncertainty can particularly benefit from the use of mechanistic biogeochemical models, which are distinguished from widely used statistical models that primarily explore long-term mean changes based on empirical relationships[1,2,17,18]. Mechanistic models enable the examination of phytoplankton diversity responses to stochastic meteorological forcing by explicitly resolving biological processes based on mathematical representations[18].

MHWs are an example of stochastic environmental change, characterized by extreme warming in s ea surface temperature (SST) that persists for days to months[19] (see Methods for the exact definition). However, current evidence of MHW impacts on phytoplankton compositional changes (e.g., harmful

algal blooms and the intrusion of warm-preferring species[20,21]) is largely derived from individual or region-specific events, limiting its generality and making it difficult to disentangle underlying mechanisms. Given these limitations, mechanistic modeling studies are essential to assess the robustness of ecological responses to MHWs. Moreover, SST anomalies exceeding the historical range now occur more frequently, intensely, and persistently, and are projected to continue in the future[22–25]. Therefore, reducing remaining uncertainties in phytoplankton trait-dependent responses to MHWs is crucial.

In this study, we investigate compositional responses of phytoplankton to MHWs using a global ocean-biogeochemical model under present-day climate conditions (MITgcm-Darwin; Methods). The model resolves 310 phytoplankton types across three trait axes: cell size, functional role, and thermal optimum. Specifically, combinations of size and functional role define 31 size–functional groups (Fig. S1). These are further subdivided into 10 temperature range preferences such that growth rates (μ_T) peaks at 0, 4, 8, …, 36 °C, respectively; this is distinct from most models where μ_T monotonically increases with temperature following the Eppley curve[26–29] (Fig. S2). Based on 15 years of simulation results, we show that MHWs can significantly disturb local phytoplankton community composition, with their impacts varying with heatwave properties and regional background environments.

Results

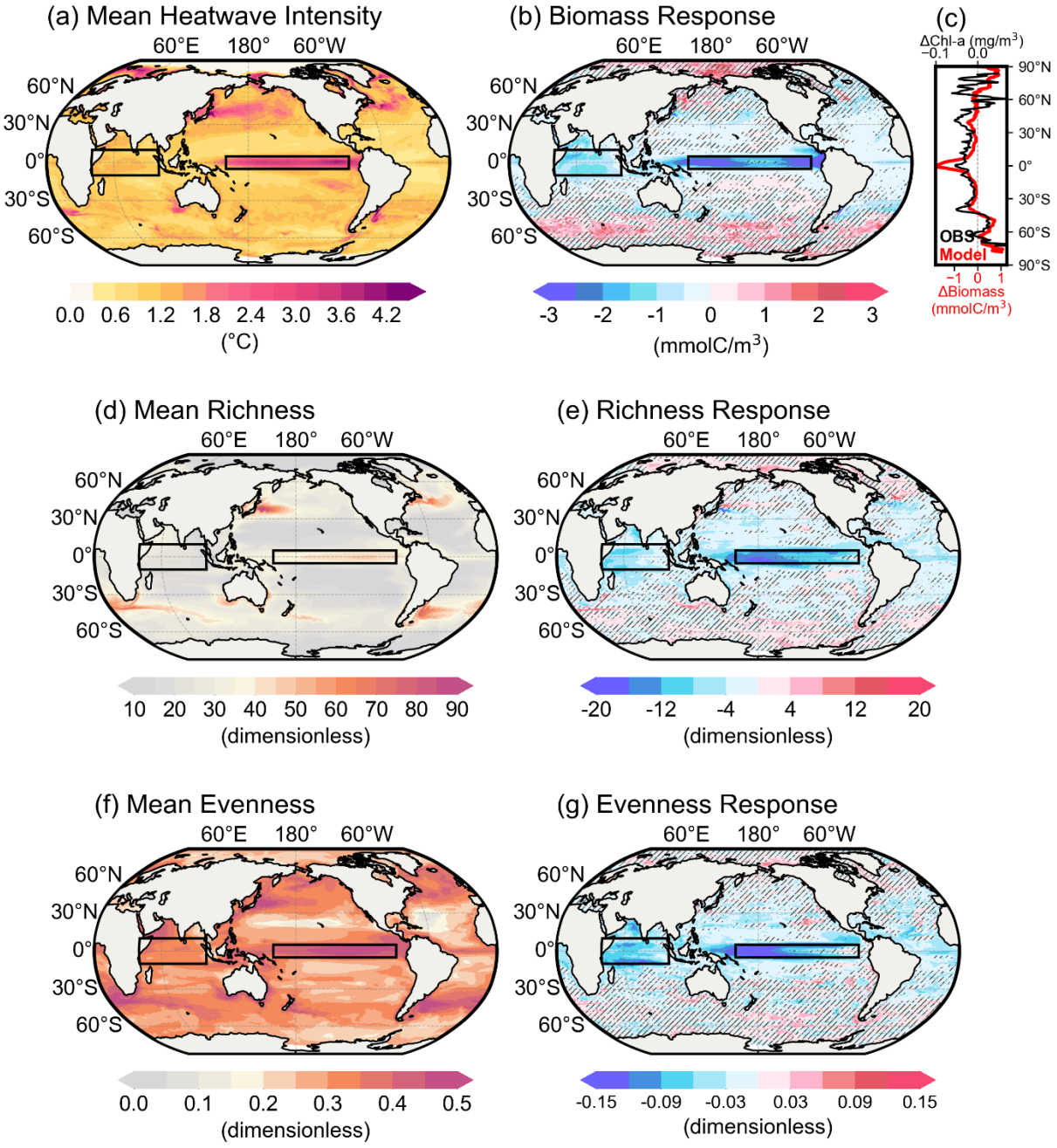

Fig. 1. General characteristics of heatwaves and phytoplankton responses simulated in the model. **a** Mean pattern of heatwave intensity (°C), defined as average SST anomalies during MHW periods (periods of extreme SST warming relative to the climatologically observed range; see Methods). **b** Biomass anomalies (mmol C m^{-3}) averaged for MHW periods. The zonally averaged biomass anomalies are shown in **c** (red). For a comparison, the zonally averaged satellite-observed Chl-*a* anomalies (mg m^{-3}) during MHW periods are presented in black. Observational Chl-*a* and SST data were obtained from OC-CCI[30,31] and the OISST dataset[32], respectively (1998-2019; Fig. S3 for the global distribution). **d, f** Simulated mean patterns of richness (the number of co-existing types, with a theoretical maximum value of 310 in this study) and evenness (higher values indicate more comparable contributions among types). **e, g** Anomalies of richness and evenness averaged for MHW periods. In the anomaly patterns,

hatched areas indicate grid points where responses are not statistically significant, indistinguishable from zero based on the 90% bootstrap confidence interval (N=1,000). Black boxes denote the Indian (40°−100°E, 10°S−10°N) and equatorial Pacific (160°E–90°W, 5°S–5°N) Oceans, which are of particular focus of subsequent analyses.

Global Responses of Phytoplankton Community to MHWs

The spatial distribution of mean heatwave intensity agrees well with observations, with the pronounced heatwaves in the western boundary current systems and ENSO region (Fig. 1a and Methods)[33,34]. The response of total phytoplankton biomass to MHWs further indicates that physical-biogeochemical interactions are also reasonably resolved in the model (Figs. 1b,c and S3). The observed negative (positive) impacts of MHWs on phytoplankton in low- to mid-latitude (high-latitude) regions are well-captured. Previous studies attributed these negative impacts to strong stratification during MHWs that inhibits vertical nutrient fluxes[4,6,35]. In high-latitude regions where nutrients are relatively abundant, instead light limitation is alleviated under increased stratification as phytoplankton spend more time in the euphotic zone, leading to higher biomass[36].

In Fig. 1d and 1f, simulated mean patterns of phytoplankton diversity are presented, measured as richness (the number of co-existing types; Methods) and evenness (the degree of uniform proportions among types). The high richness in the equatorial Pacific reflects the co-existence of multiple size classes, driven by the combined effects of size-dependent grazing and high nutrient supply from below[12]. In western boundary current systems and turbulent zones in the Southern Ocean, strong mixing plays a key role in maintaining phytoplankton communities with diverse temperature preferences[12,37,38]. These regions generally exhibit high evenness, indicating biodiversity hotspots characterized by relatively well-balanced community composition. A positive relationship between richness and evenness in marine autotrophs has also been reported at a species level[39], potentially due to the “rescue” effect that prevents species that are not locally well adapted from going extinct and thereby maintain high evenness. Our results suggest that similar mechanisms may apply in the trait space under climatological conditions.

During MHWs, richness anomalies show a similar latitudinal contrast to total biomass, although

positive anomalies in high-latitude areas are weaker (Fig. 1b,e). Significant negative anomalies are observed primarily in the equatorial Pacific and Indian Ocean, whereas other biodiversity hotspots in higher latitudes exhibit more heterogeneous and statistically less significant responses. The latter indicates the influence of local small-scale processes associated with transport and mixing, while also possibly reflecting limited representation of MHW-associated shortwave effects in the biogeochemical model (see Methods and the Summary and discussion section). Evenness responses largely follow those of richness (Fig. 1g). Substantial decreases in both indicators in equatorial oceans demonstrate that MHWs not only lead to a temporary loss of certain types (reducing richness) but also reorganize the remaining structure to become less balanced (reducing evenness). These results suggest that MHWs disproportionately impact phytoplankton with different traits, motivating further examination of the compositional changes in these regions.

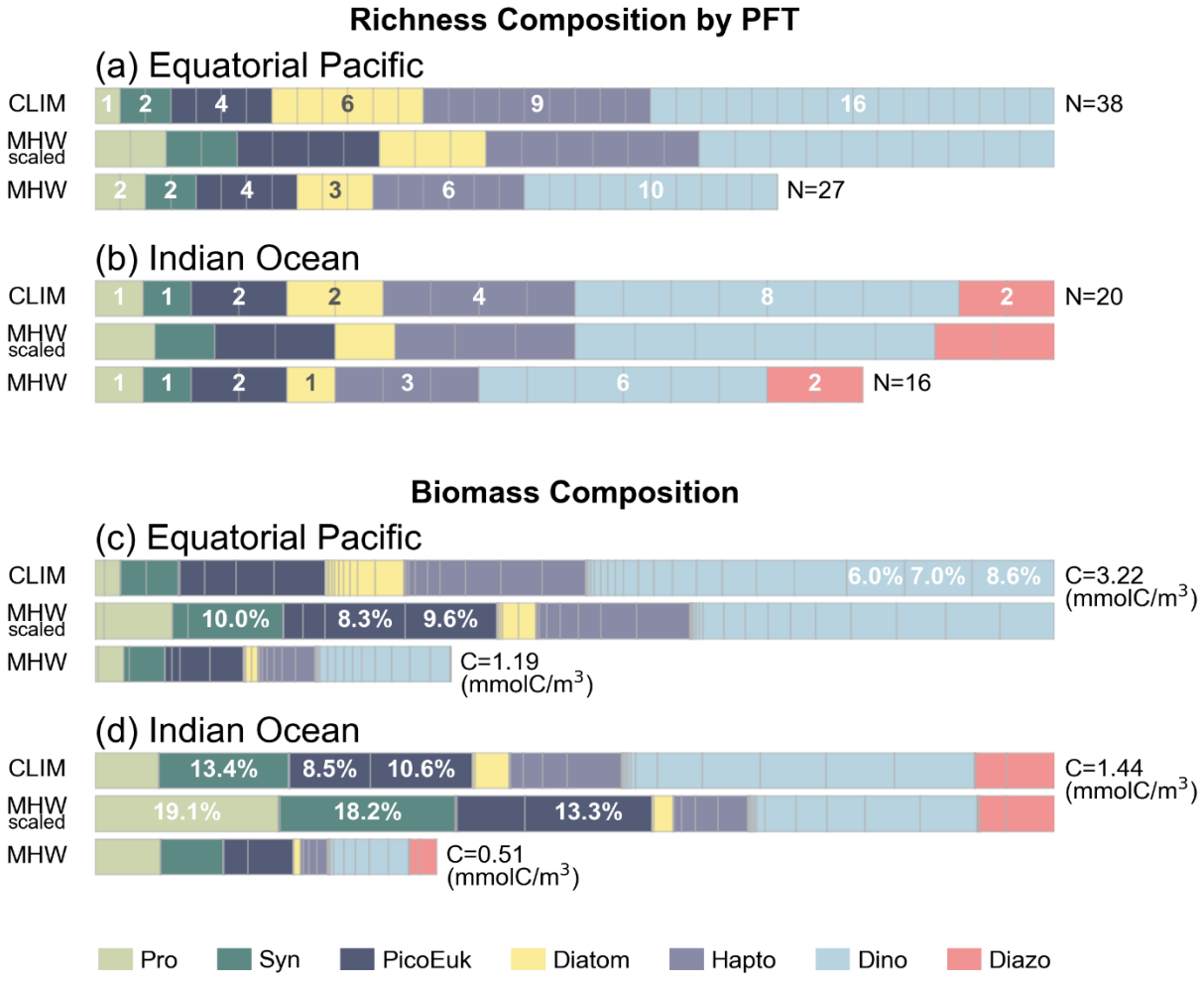

Fig. 2. Phytoplankton Community Composition for Selected Regions. a,b Richness compositions for the (**a**) equatorial Pacific and (**b**) Indian Ocean. In each panel, 'CLIM' (top) and 'MHW' (bottom) denote compositions under the climatological and MHW conditions, respectively. The analysis was first conducted at the grid-point level (that is, for each model grid cell, climatological and MHW-conditioned compositions were obtained by averaging along the time dimension), and then averaged over each domain (black boxes in Fig. 1). Colors represent PFTs, as indicated by the legend (Pro: *Prochlorococcus*, Syn: *Synechococcus*, PicoEuk: Picoeukaryote, Hapto: Haptophyte, Diazo: Diazotroph, Dino: Dinoflagellate). Within each color, the number of rectangles outlined in grey corresponds to the PFT-specific richness (rounded to the nearest integer), also displayed as numbers on the bars. The total richness is shown at right (*N*). The middle bar corresponds to the 'MHW' composition but is scaled to climatological totals, allowing comparison of PFT percentages and highlight compositional changes ('MHW scaled'). **c,d** Similar to **a,b**, but for biomass composition. The length of each element (outlined in grey) is proportional to the biomass concentration (mmol C m^{-3}) of a given type. 'C' denotes the total biomass summed over all existing types. For visual clarity, percentages are shown only for the top three dominant types.

Composition changes in the equatorial Pacific and Indian Ocean

Fig. 2 shows phytoplankton community structure in the equatorial Pacific and Indian Ocean,

grouped by phytoplankton functional types (PFTs; *Prochlorococcus*, *Synechococcus*, picoeukaryote, diatom, haptophyte, dinoflagellate, and diazotroph). In the equatorial Pacific, an average richness of 38 decreases to 27 under MHW conditions (~30% reduction). This diversity loss is driven by the disappearance of several taxa within dinoflagellate, haptophyte, and diatom groups, which contribute most to the climatological richness. By comparison, richness of pico-sized phytoplankton (*Prochlorococcus*, *Synechococcus*, and picoeukaryotes) is less affected by MHWs. *Prochlorococcus* even shows an increase in richness, partially offsetting the overall decline. For each PFT, richness during MHWs differs significantly from climatological values, based on 90% bootstrap confidence intervals (N = 5,000; Methods and Table S1). These changes result in an increased proportion of picophytoplankton to the total community richness (comparing top and middle bars in Fig. 2a).

Beyond presence–absence information, we also examine the biomass composition in this region (Fig. 2c). During the climatological period, dinoflagellates appear as the most dominant PFT, followed by haptophytes and picoeukaryotes. Although this is somewhat different from in-situ observations that reported a predominance of picophytoplankton for this region[40–42], recent satellite-based estimates of phytoplankton size classes suggest a substantial fraction of nano- and micro-phytoplankton in the equatorial Pacific, lending support to the simulated dominance of larger phytoplankton (Fig. S4).

Biomass responses during MHWs clearly show a shift toward smaller phytoplankton, with enhanced contribution of picophytoplankton to the total biomass. Such shifts in size structure can arise from bottom-up control: smaller phytoplankton have higher nutrient uptake efficiency, due to their high surface area-to-volume ratio and thin outer layers[43,44]. This gives them a competitive advantage under the reduced nutrient supply by enhanced stratification during MHWs (Fig. S5a-c). At the same time, top-down control can operate through grazing-mediated coexistence, where the existence of large phytoplankton depends on the degree of grazing pressure on small phytoplankton[12,45,46]. During MHWs, grazing pressure on pico- and nano-phytoplankton is weakened (Fig. S6), hence favoring the dominance of smaller-sized phytoplankton. Given that nutrient concentrations are directly modulated by MHWs, whereas zooplankton responses are mediated through phytoplankton, bottom-up control is likely the

primary driver of the shift toward smaller types. The resulting alterations in prey–predator interactions further reinforce this size structure. Consequently, evenness declines, as reflected in the increased contribution of the top three dominant types (21.6% to 27.9%). In addition, the Bray–Curtis dissimilarity[47], which quantifies differences between two compositions on a scale from 0 (identical) to 1 (non-overlapping compositions), was measured to be 0.489 ± 0.001 (Methods). Compared to dissimilarities expected for mean compositional changes under global warming (~0.2)[14], the higher value under MHW conditions indicates that MHW-induced shifts in the community composition can be substantial, albeit transient.

These overall features also hold for the Indian Ocean. The trait diversity decreases by ~20% from 20 to 16 under MHW conditions, primarily in dinoflagellates, haptophytes, and diatoms (Fig. 2b). The relative contribution of picophytoplankton increases for both total richness and total biomass (Fig. 2d), with a decrease in evenness (Fig. 1g). The Bray–Curtis dissimilarity between the climatology and MHW compositions in the Indian Ocean is 0.478 ± 0.001, reflecting significant compositional changes during MHWs. A distinct feature relative the Pacific is that in the Indian Ocean, picophytoplankton and nitrogen-fixing diazotrophs are relatively abundant for both climatological and MHW conditions. These features reflect the low background dissolved inorganic nitrogen (DIN) concentrations (Fig. S5b), as diazotrophs can fix atmospheric N_2 and are therefore not limited by low DIN, gaining a competitive advantage.

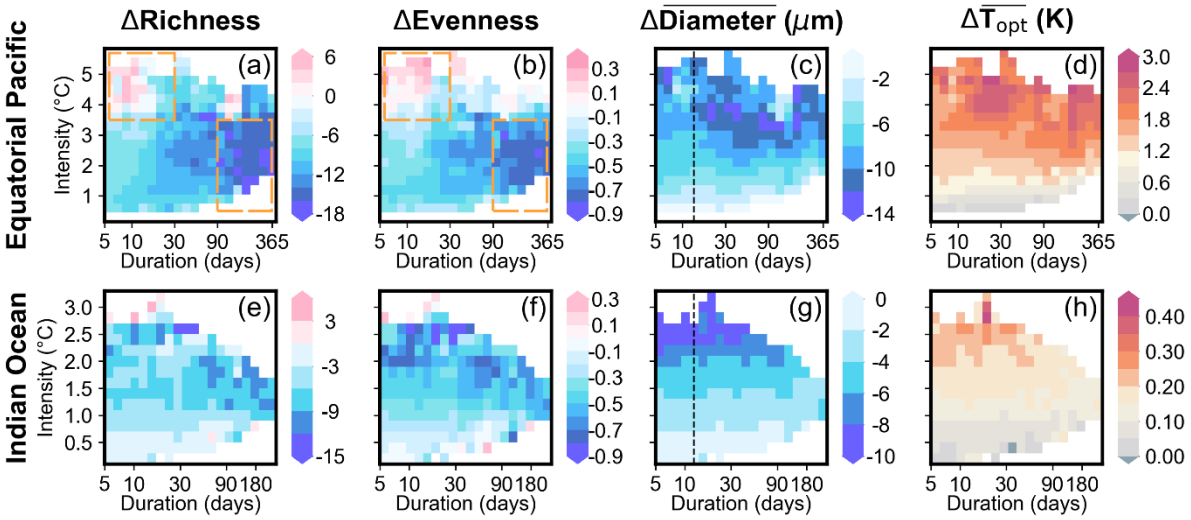

Fig. 3. Phytoplankton community characteristics as a function of MHW intensity and duration. Upper panels correspond to the equatorial Pacific (**a-d**) and lower panels to the Indian Ocean (**e-h**). Each column represents anomalies in (**a,e**) richness, (**b,f**) evenness, (**c,g**) community-mean cell diameter ($\Delta\bar{d}$), and (**d,h**) community-mean optimal temperature ($\Delta\overline{T_{opt}}$). Community means are defined as biomass-weighted averages; examples for diameter corresponding to the black dashed lines in **c,g** are provided in Fig. S7. The domains of short and strong (SS-MHWs) and long and moderate heatwaves (LM-MHWs) are highlighted by orange dashed lines in **a,b**. Heatwave events were identified at individual grid cells, yielding 207,726 and 245,064 events in the equatorial Pacific and Indian Ocean, respectively (see Fig. S8 for sample sizes considered in each intensity–duration bin).

Effects of Heatwave Characteristics

Next, we examine whether phytoplankton responses vary with heatwave characteristics. Phytoplankton community properties are evaluated using four indicators: richness, evenness, biomass-weighted mean cell diameter ($\bar{d}$), and biomass-weighted mean optimal temperature ($\overline{T_{opt}}$). Note that $\overline{T_{opt}}$ in this study is equivalent to the community temperature index (CTI), a widely used metric of community temperature preference[48]. Interestingly, Fig. 3a-b reveals increased biodiversity during short and strong heatwaves (SS-MHWs; duration < ~30 days and intensity > 3.5 °C) in the equatorial Pacific, which was not evident in Fig. 1. This contrasts with the substantial negative response under long and moderate heatwaves (LM-MHWs; duration > 90 days intensity < 3.5 °C), suggesting that both intensity and duration play a role in modulating biodiversity changes. By comparison, size structure, represented by $\bar{d}$, is more closely related to heatwave intensity, reflecting the strong influence of heatwave intensity

on nutrient supplies (Fig. S5d). $\overline{T_{opt}}$ also strongly depends on heatwave intensity, as expected. This is a result that could only be shown by the setup used here as most models assume only a monotonic relationship between μ_T and temperature[26–29] (Fig. S2).

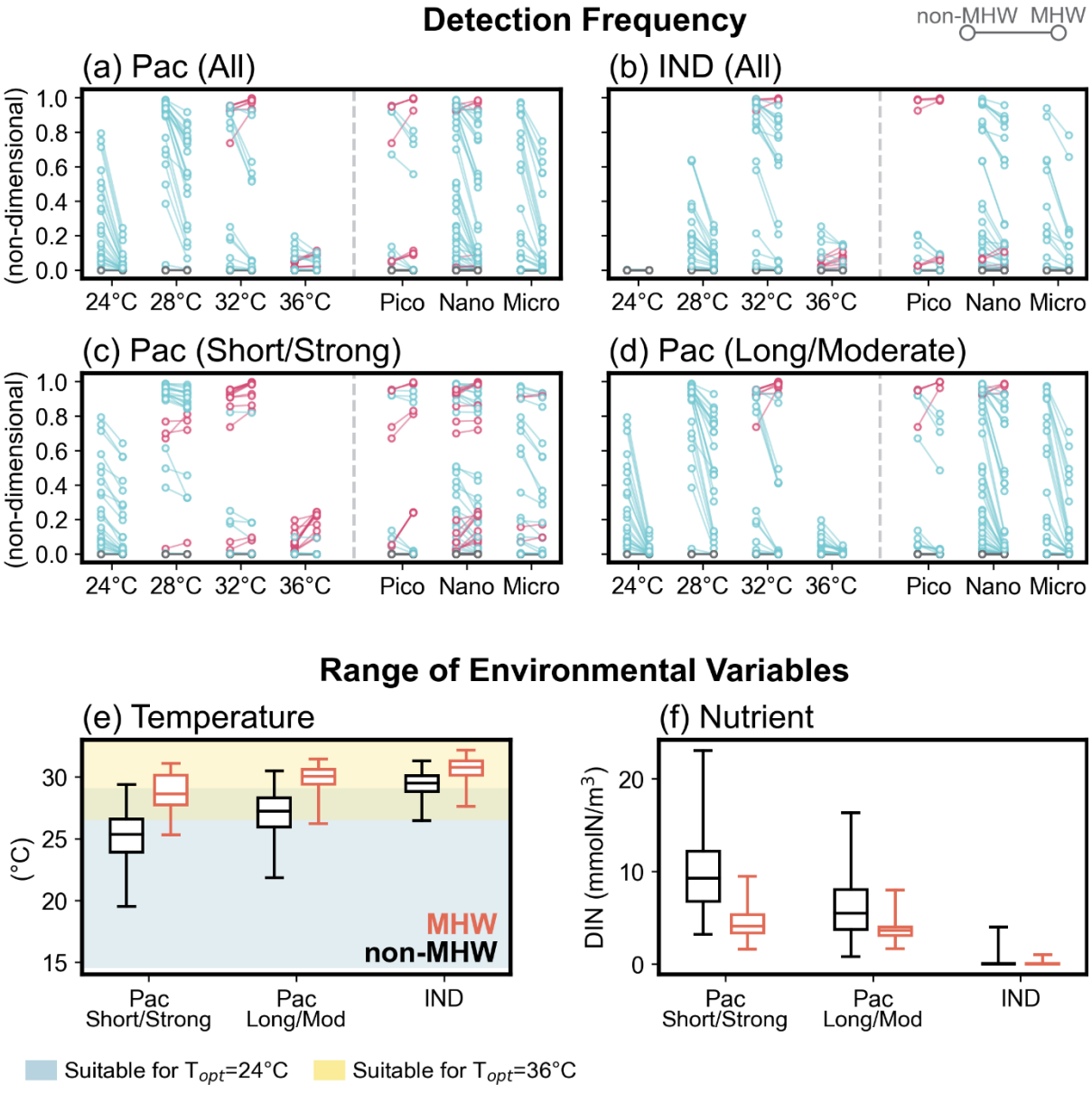

Fig. 4. Comparison of detection frequency and environmental conditions between non-MHW and MHW periods. a-d Each pair of connected dots represents the detection frequency of an individual phytoplankton type under non-MHW condition (left dots) and MHW condition (right dots). Detection frequency during non-MHW periods was calculated at each grid point as the number of non-MHW days with the presence of a given phytoplankton type divided by the total number of non-MHW days, and then averaged over the corresponding area. For the Pacific sub-cases (**c,d**), the areas correspond to grid

cells where heatwaves of the corresponding category occurred at least once (Fig. S9). The same procedure was applied to MHW periods. Results are grouped by optimal temperature (left of the dashed line) and by size class (right of the dashed line). Note that those with optimal temperature below 24 °C are not found in either region. Increases in detection frequency during MHW periods are highlighted in red, and decreases in blue. Cases where MHWs do not lead to significant changes in detection frequency are shown in grey; these are identified by overlapping 90% bootstrap confidence intervals between non-MHW and MHW values. **e-f** Distributions of area-averaged temperature (°C) and DIN concentration (mmol m^{-3}) are shown as box plots. For equatorial Pacific, areas experiencing each heatwave category are displayed separately. Each horizontal break indicates the 1st percentile, 25th percentile, mean, 75th percentile, and 99th percentile, from bottom to top. Non-MHW and MHW periods are distinguished by color. In **e**, suitable temperature ranges for P24 and P36 are marked by shading, defined as the *e*-folding range around the maximum growth rate in the temperature–growth rate function.

Further analysis of detection frequency, defined as the fraction of MHW (non-MHW) days with the presence of a specific type relative to the total MHW (non-MHW) days, shows that elevated richness during SS-MHWs arises primarily from increased detection of pico- and nano-sized phytoplankton with warmer temperature preferences (Fig. 4c). These include climatologically rare types, whose appearance during MHWs also contributes to increased evenness (Fig. 3b). This pattern is associated with the underlying environmental conditions. As implied by Fig. 1a, intense heatwaves mainly occur in the eastern equatorial Pacific (Fig. S9a). In this region, the mean temperature is relatively low (25.1 °C, Fig. 4e) due to strong upwelling driven by the trade winds (the Bjerknes feedback)[49] and is close to the thermal optimum of 24 °C-preferring types (referred to here as 'P24'). However, SST increases to 28.7 °C during SS-MHWs, which then includes the suitable range for the 36 °C-preferring types ('P36') while remaining tolerable for the relatively cooler-preferring types like P24. At the same time, DIN concentrations remain around 4.4 mmol m^{-3} during MHWs (Fig. 4f), above the 4 mmol m^{-3} level that is considered nutrient-rich[50]. Therefore, the negative impact of reduced nutrients on phytoplankton is limited, particularly given the short duration of these events, and does not outweigh increased diversity by temperature. As a result, the emergence of P36, together with a moderate reduction in P24, contributes to the shift toward higher $\overline{T_{opt}}$ (Fig. 3d).

By comparison, regions experiencing LM-MHWs are characterized by higher mean temperatures, located farther from the core of equatorial upwelling (Figs. 4e and S9b). In these regions, the mean temperature of 27.0 °C during non-MHW periods lies within a suitable range for both P24 and P36.

However, an SST rise to 29.9 °C during MHWs leads to an environment that is no longer suitable for P24 (shadings in Fig. 4e). This causes drastic decreases in detection frequencies of P24 (Fig. 4d), resulting in a rise in $\overline{T_{opt}}$. Nonetheless, temperature alone cannot fully account for the overall declines in detection frequencies across all temperature traits, given that the anomalous warming can be favorable for warmer-preferring types. Among other environmental factors, light availability is unlikely to be limited in the equatorial region, indicating nutrient limitation as the plausible factor. As expected, DIN concentrations significantly decrease under LM-MHW conditions from 6.2 mmol m^{-3} to 3.7 mmol m^{-3} (Fig. 4f). This not only falls below the nutrient-rich criterion but also persists for more than 90 days, imposing sustained stress on the phytoplankton community across traits. Therefore, the pronounced diversity loss during LM-MHWs arises from the combination of (i) a thermal niche contraction negatively affecting P24 and (ii) a prolonged nutrient deficit that is particularly disadvantageous for large phytoplankton but ultimately affects all trait groups. The net response to all heatwaves is dominated by this diversity decline, likely due to the larger spatial extent of LM-MHW than SS-MHW events (Fig. 4a).

Diversity responses in the Indian Ocean are more straightforward, with stronger and longer heatwaves generally being associated with greater reductions in diversity (Fig. 3e-h). Consistent with the Pacific, the size structure ($\bar{d}$) and $\overline{T_{opt}}$ strongly depends on heatwave intensity, with the former reflecting modulation of heatwave intensity on nutrient anomalies (Fig. S5e). Although some warm-preferring types benefit from elevated SST during MHWs (thus contributing to warmer $\overline{T_{opt}}$), decreases in detection frequencies across temperature traits indicate that nutrient stress plays a more dominant role in reducing phytoplankton diversity (Fig. 4b). In this oligotrophic region, where mean DIN concentration is 0.24 mmol m^{-3} under non-MHW conditions, a further decline to 0.04 mmol m^{-3} during MHW conditions may substantially suppress total biomass across traits, particularly larger types, leading to the loss of certain taxa and a consequent decline in richness.

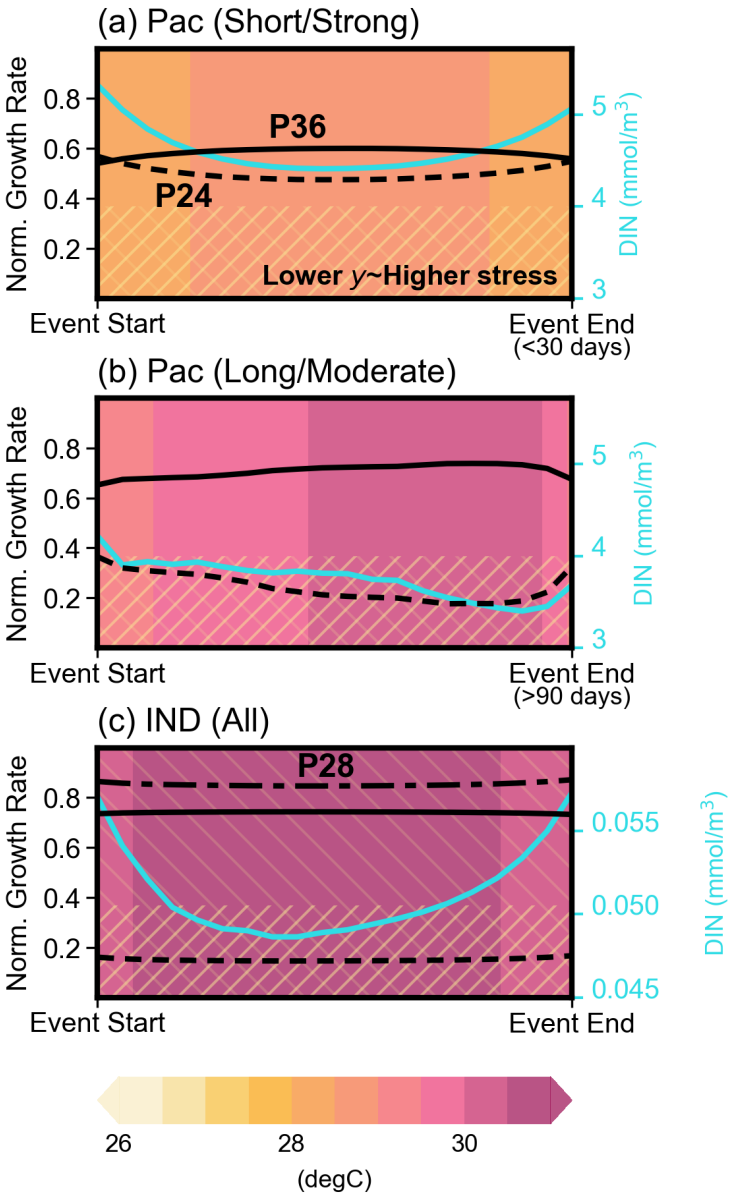

Fig. 5. Time evolution of physical variables during heatwave events. Physical variables are composited for each heatwave category and aligned by event onset and termination. Shading represents SST (°C). Black lines show the corresponding μ_T for phytoplankton with different temperature preferences, calculated from the prescribed temperature–μ_T relationships (Fig. S2b): dashed lines for P24, solid lines for P36, and dash-dotted line for 28 °C-preferring type ('P28'; Indian Ocean only). Each μ_T curve is normalized by μ_T at the optimal temperature (i.e., the maximum) so that they range between 0 and 1. The bright blue line indicates DIN concentration (mmol m^{-3}). Slash-hatched areas (/) indicate high thermal stress, where normalized μ_T is lower than e^{-1}. Backslash-hatched areas (\) indicate conditions with DIN < 4 mmol m^{-3}. **a** SS-MHWs in the equatorial Pacific. **b** LM-MHWs in the equatorial Pacific. **c** Indian Ocean.

Summary and Discussion

Responses of phytoplankton diversity to MHWs were examined using an advanced ocean-biogeochemical model, that resolves trait-based phytoplankton dynamics in spatially and temporally continuous fields across the global ocean. The results show a slight increase in biodiversity at high latitudes and mixed responses in biodiversity hotspots during MHWs. This contrasts to a large-scale, systematic decrease at low latitudes, particularly the equatorial Pacific and Indian Ocean. Focusing on these tropical regions, this study shows that the decrease in diversity is primarily attributed to loss of large taxa with low thermal optima under MHW-induced warm, low-nutrient conditions. The competitive advantage of small phytoplankton is further strengthened through prey–predator interaction feedback, significantly reducing community evenness.

The detailed responses vary with heatwave characteristics and environmental conditions. During SS-MHWs in the equatorial Pacific, SST does not exceed the thermal range suitable for most existing types and nutrient stress remains moderate due to strong upwelling conditions (Fig. 5a). Consequently, diversity loss is limited, while relaxation of thermal stress on types that are rare under non-MHW conditions increases their occurrence, ultimately increasing both richness and evenness. On the other hand, LM-MHWs mainly occur in the warmer parts of the equatorial Pacific, where anomalous warming exerts significant heat stress on many existing phytoplankton types (Fig. 5b). Further, nutrient stress accumulates under prolonged conditions, as indicated by the delayed negative peak of DIN concentrations (cyan line, Fig. 5b). These combined effects of thermal and nutrient stress result in a significant decrease in diversity. Finally, in the Indian Ocean where mean SST is already high and MHW-induced warming typically reaches ~1°C, heatwaves do not significantly alter thermal habitat suitability (Fig. 5c). Instead, the oligotrophic background state makes the phytoplankton community susceptible to reduced nutrient fluxes, leading to a loss of diversity.

Several inherent limitations should be acknowledged. First, climate–biogeochemical interactions are resolved one-way in the model, leaving uncertainties in potential feedbacks to the climate system, including upper-ocean radiative heating[51] and biogenic emissions that contribute to cloud condensation

nuclei[52]. These processes may further modulate biological responses, especially for long heatwaves that allow sufficient time for feedbacks to develop. Second, MHW-associated light limitation effect is only partially represented by the model, accounting for stratification-mediated changes in light availability (indirect effect) but not variations in the incoming shortwave radiation (direct effect) (Methods). However, incorporating the direct effect may not substantially change our main conclusions, since the tropical regions highlighted here are not light-limited at the surface. Also, MHWs do not exhibit systematic relationships with shortwave radiation[35]. This suggests that thermal and dynamical forcings of MHWs are the primary pathways that shape phytoplankton composite responses, and these processes are well-captured by the model. Finally, despite the advanced configuration of 310 phytoplankton types, the lack of several ecologically important trait dimensions (e.g., cell shape, coloniality) impose limitations on fully representing the climate–ecosystem interactions. Inclusion of additional traits could further refine community responses by influencing sinking velocities and prey preferences. Nonetheless, the agreement between observational and simulated results (Fig. 1b,c) indicates that the key dynamics of climate–ecosystem interactions are successfully captured in this study.

Phytoplankton compositional changes can have cascading impacts on marine ecosystem functions through multiple pathways. For instance, phytoplankton diversity has been linked to community productivity through complementarity (e.g., resource partitioning by diverse taxa) and selection (likelihood of high-productivity taxa) effects[53]. Size structure is also an important factor for the carbon export efficiency, as it influences sinking rates[54] and the number of trophic transfer steps before the carbon reaches to the deep ocean[7,8,55]. The diversity losses and shifts toward smaller types shown in this study suggest a potential decrease in the biological carbon pump. At the same time, alterations in food web dynamics can also affect fisheries and aquaculture production[10]. These consequences are likely to interact with the broader, warming-driven reorganization of phytoplankton communities under anthropogenic climate change. Such changes, however, are often masked when considering total abundance alone. Therefore, improving our understanding of trait-dependent phytoplankton dynamics is crucial for predicting future changes in the marine ecosystem.

Methods

Marine Heatwave Analysis

MHWs are defined as periods during which SST exceeds the climatological 90th percentile for five or more consecutive days[19,33]. The 90th percentile threshold was calculated using an 11-day window centered on each calendar day. MHWs were identified at each model grid cell using the Python module 'marineHeatWaves' (https://github.com/ecjoliver/marineHeatWaves). MHW intensity was measured as SST anomalies averaged for each event. In the composite analysis, anomalies were averaged across all days identified as MHW events, and then area-averaged when necessary (e.g., Fig. 2). In our 15-year simulation, the minimum number of MHW events detected at a single grid point was ten in the equatorial Pacific and Indian Ocean (five in the global domain; Fig. S10a). In Fig. S10b, simulated mean durations of heatwave events are also shown.

Model and Experimental Configurations

In this study, the MIT general circulation model[56] (MITgcm) is used to simulate physical oceanic processes over the global domain with the LLC270 grid configuration[57], which is eddy-permitting and has a horizontal resolution of approximately 1/3° at the equator and ~18 km at high latitudes. Vertical grids are distributed from the surface to 6,135 m over 53 layers, representing an extension of the standard LLC270 configuration (50 layers); the 10 m thick top layer of the standard configuration is further subdivided into four sub-layers with the thickness of 2 m, 2 m, 3 m and 3 m. The layer thickness increases from 2 m at the surface to several hundred meters in the bottom layer.

The driving atmospheric forcing was derived from a separate coupled atmosphere–ocean general circulation model simulation (the "present-day" simulation with CESM). In this simulation, the atmospheric CO_2 concentration was fixed at 367 ppm, approximately representing year-2000 levels. This atmospheric field was adopted for the following two primary reasons: (i) to establish a fundamental

364 understanding of MHW impacts on phytoplankton community composition while excluding long-term
365 global warming effects; and (ii) to facilitate future comparisons with higher-CO_2 simulations. The initial
366 conditions for oceanic fields were obtained from a previously conducted hindcast simulation that was
367 initialized based on ECCO product[58,59] and were therefore already adjusted to present-day climate
368 conditions. Thereafter, the physical component was integrated for four years as a spin-up before
369 coupling with the biogeochemical model.

370 The biogeochemical fields resolved by Darwin[60] are transported and mixed by the physical
371 component of the simulation. However, biogeochemical processes do not affect the physical component;
372 thus, potential feedback processes from phytoplankton dynamics to the physical climate system are not
373 simulated. Details of the mathematical formulation of Darwin can be found in ref. [61]. Here, we briefly
374 present the equation describing the temporal evolution of phytoplankton concentration:

$$\frac{\partial P_i}{\partial t} = \underbrace{-\nabla \cdot (\mathbf{u} P_i)}_{\text{advection}} + \underbrace{\nabla \cdot (\mathbf{K} \nabla P_i)}_{\text{diffusive mixing}} + \underbrace{S_{P_i}}_{\substack{sources \\ and\ sinks}} . \quad (1)$$

375 In the equation, P_i denotes the mass concentration of phytoplankton with i=1, …, 310 representing
376 the trait-based types used in this study. The velocity vector is given by $\mathbf{u}$, and $\mathbf{K}$ denotes the directional
377 mixing coefficients. The terms on the right-hand side correspond to advection, mixing, and source–sink
378 processes, respectively. The last term is further expanded as follows:

$$S_{P_i} = \underbrace{\mu_i P_i}_{Growth} - \underbrace{m_i P_i}_{Mortality} - \underbrace{\sum_k g_{ik} Z_k}_{Grazing\ loss} - \underbrace{\frac{\partial(\omega_{P_i} P_i)}{\partial z}}_{Sinking} \quad (2)$$

379 The growth rate μ_i is formulated as a function of nutrients, temperature, irradiance, with parameters
380 specific to each phytoplankton type. Mortality is parameterized by a temperature-dependent coefficient,
381 m_i. Pairwise grazing interactions between phytoplankton type i and zooplankton type k are represented
382 by the coefficient g_{ik}, and Z_k indicates the biomass of the k-th zooplankton type (k=1, …, 16). The
383 sinking velocity ω_{P_i} is also type-specific.

384 Phytoplankton are resolved into 310 types defined by three traits: phytoplankton biogeochemical

functional type (PFT), cell diameter, and temperature norm (Fig. S1). There are 31 groups distinguished by combinations of PFT and cell size. The two smallest are analogues of *Prochlorococcus* and *Synechococcus*. These are followed by picoeukaryotes analogues with two size classes. The prokaryotes and these two pico-eukaryotes are classified as picophytoplankton (diameter < 2 μm). Haptophytes, primarily composed of calcifying coccolithophores, are represented by five size classes of nanophytoplankton (diameter between 2–20 μm). Nitrogen-fixing diazotrophs also comprise five nano-size classes. Diatoms, characterized by siliceous shells and typically associated with rapid growth, and enhanced carbon export efficiency, are resolved into nine size classes. Finally, mixotrophic dinoflagellates occupy the largest size range with eight size classes. Sizes of diatoms and dinoflagellates range from nano- to microphytoplankton classes (diameter > 20 μm). Each of these PFT–size groups are further divided into 10 types with distinct thermal ranges and optimal temperatures, yielding a total of 31 × 10 = 310 types. The thermal optima are prescribed approximately from 0 to 36 °C at 4 °C intervals (Fig. S2a), covering the range of observed SST.

Other PFT-specific parameters in the model include the limiting nutrient (e.g., Si for diatoms), the maximum carbon-specific growth rate, palatability to predators (there are 16 zooplankton types defined by size class), and the absorption spectrum. To incorporate the PFT-specific absorption spectra, shortwave radiation must be prescribed in discrete wavelength bands. However, as CESM does not explicitly resolve wavelengths, an alternative input is required. We applied monthly varying output from the Ocean–Atmosphere Spectral Irradiance Model (OASIM)[62] under present-day conditions. With this implementation, the sum of wavelength-dependent radiation used by phytoplankton in the biogeochemical model does not necessarily match the solar radiation used to heat the upper ocean in the physical model. At the level of individual events, this may lead to either intensified or alleviated light limitation relative to that implied by the physical model. However, the net effect is likely minimized in the composite analysis. In addition, MHWs do not exhibit a systematic relationship with shortwave radiation[35], and the regions we highlight in this study are not light limited at the surface. Therefore, the observed biological responses to MHWs can be primarily attributed to thermal and

411 nutrient stress, which are successfully captured in the model.

412 The overall model configurations largely follow those of ref. 12. A major difference lies in the higher
413 spatial resolution employed in this study (1/3° instead of 1°). Higher resolution has generally been
414 associated with a better representation of boundary currents, fronts, and equatorial currents as well as
415 MHW phenomena[63–65]. In addition, atmospheric forcing in the previous study was annually repeated,
416 whereas the CESM-derived forcing here includes interannual variability. This enables a comparison of
417 local biogeochemical responses under MHW and non-MHW conditions, ensuring the robustness of the
418 results by accounting for stochastic variability. Following the physical spin-up, the model was
419 integrated for an additional four years for biological adjustments. Given the high computational cost of
420 the model, we used the outputs from ref. 12 as the initial condition to minimize the spin-up time. The
421 analysis was performed for 15 years of integration following this adjustment period.

422

423 **Biodiversity metrics**

424 This study primarily focuses on α-diversity, which represents biodiversity within a local community
425 at a given time. It was evaluated using two widely used indicators—richness and evenness. Richness is
426 measured as the number of species present in the community. In this study, however, it was measured
427 at the phytoplankton type level rather than at the species level, with a maximum possible value of 310.
428 Evenness (J) is defined following Pielou's index[66]:

$$J = \frac{-\sum_i p_i \ln p_i}{\ln S}. \quad (3)$$

429 Here, p_i denotes the biomass fraction of the i-th phytoplankton type and S is the total number of types
430 (richness). High evenness indicates a more uniform distribution of biomass across types, whereas low
431 evenness reflects dominance by a few types.

432 We also assessed Bray–Curtis dissimilarity to quantify differences between two communities (β-
433 diversity)[47]:

$$BC = 1 - \frac{2\sum_i \min\left(B_i^1, B_i^2\right)}{\sum_i \left(B_i^1 + B_i^2\right)}, \quad (4)$$

where B_i^n is the biomass of i-th phytoplankton type, with $n = 1$ and $n = 2$ referring to the climatological and MHW-averaged communities, respectively. The Bray–Curtis dissimilarity equals 0 when the two compositions are identical, and the highest value of 1 indicates that the two communities share no types.

Resampling of Community Composition for Significance Testing

To investigate whether the composition during MHWs is significantly different from that of the climatology (Fig. 2), we performed bootstrap resampling tests as follows. For each grid point, richness was calculated for each PFT at every time step, yielding seven time series of PFT-specific richness. The climatological composition ('CLIM' in Fig. 2a,b) was derived by taking the time and area averages of these time series. To determine confidence intervals of the MHW-period composition, MHW events at each grid point were resampled 5,000 times (N) maintaining the original number of events and allowing replacement. This procedure generated grid-wise pseudo-compositions (that is, PFT-specific richness averaged over the resampled MHW time steps). After area-averaging these pseudo-compositions, confidence intervals were estimated using the corresponding percentile values. For all PFTs, the confidence intervals of the MHW-period compositions did not encompass the climatological values. Although the numbers shown in Fig. 2a,b appear identical for some PFTs (e.g., 'Syn' and 'PicoEuk') under climatological and MHW conditions due to rounding, their difference is statistically significant (Table S1).

For the Bray–Curtis dissimilarity, MHW events were first resampled using a bootstrap method (N = 5,000) to generate pseudo-compositions for MHW conditions. Each pseudo-composition was paired with the climatological composition, yielding 5,000 Bray–Curtis dissimilarity values. The climatological composition is fixed across all pairs, assuming negligible sampling uncertainty given its large sample size (365 days × 15 years = 5,475). Confidence intervals were assessed using 10th and 90th percentiles. In the main text, we present a qualitative comparison of Bray–Curtis dissimilarities

between our results and those from a previous study that investigated a global warming scenario[14]. However, a direct comparison was not straightforward, as they employed a 35-phytoplankton type configuration, although it was based on the same biogeochemical model (Darwin). Given that their classification is largely comparable to the 31 PFT–size groups in this study (without considering optimal temperature traits), we recalculated Bray–Curtis dissimilarities using a 31-group framework. This yielded values of 0.465 for the equatorial Pacific and 0.478 for the Indian Ocean. Although the relative magnitude between the Pacific and Indian Oceans is reversed compared to the 310 framework, the qualitative feature that MHW-driven transient perturbations in community composition tend to be larger than long-term shifts under global warming remains consistent.

Data Availability

The code of Darwin is available at https://github.com/darwinproject/darwin3, MITgcm at https://github.com/MITgcm-contrib/llc_hires/tree/master/llc_270, and the module 'marineHaeatWaves' at https://github.com/ecjoliver/marineHeatWaves. OC-CCI chlorophyll products can be downloaded from https://catalogue.ceda.ac.uk/uuid/b0ec72a28b6a4829a33ed9adc215d5bc/, and OISST from https://www.ncei.noaa.gov/products/optimum-interpolation-sst. The simulated data used in this paper are available at https://figshare.com/s/db9fc3f7f067c4069366[67].

Code Availability

Codes are available at https://figshare.com/s/db9fc3f7f067c4069366[67].

Acknowledgement

This study was supported by the National Research Foundation of Korea (NRF) grant funded by the Korea government (MSIT) (RS-2025-00520839, 2022R1A2C1009792), Korea Institute of Science and Technology Information (KISTI) (KSC-2024-CRE-0266), the Korea Research Environment Open NETwork (KREONET), and the Supercomputing Laboratory at King Abdullah University of Science

and Technology (KAUST). SD and OJ acknowledge support from the Simons Collaboration on Computational Biogeochemical Modeling of Marine Ecosystems (CBIOMES 549931).

Contributions

H.-J. K. and H. S. conceived and coordinated the study. H.-J. K. performed the analysis and wrote the manuscript. S. D. provided biological expertise and together with O. J. contributed to model configuration and parameterization. I. H. and Y. W. provided technical support for model implementation and simulations. S. A. and J. L. contributed to the interpretation of the results. All authors participated in the scientific discussion and contributed to the revision of the manuscript.

Competing Interests

The authors declare no competing interests.

References

1. Righetti, D., Vogt, M., Gruber, N., Psomas, A. & Zimmermann, N. E. Global pattern of phytoplankton diversity driven by temperature and environmental variability. *Sci. Adv.* **5**, 1–11 (2019).
2. Busseni, G. *et al.* Large scale patterns of marine diatom richness: Drivers and trends in a changing ocean. *Global Ecology and Biogeography* **29**, 1915–1928 (2020).
3. Vellend, M. *Conceptual Synthesis in Community Ecology*. (2010).
4. Hayashida, H., Matear, R. J. & Strutton, P. G. Background nutrient concentration determines phytoplankton bloom response to marine heatwaves. *Glob. Chang. Biol.* **26**, 4800–4811 (2020).
5. Chavez, F. P. *et al.* Biological and Chemical Response of the Equatorial Pacific Ocean to the 1997-98 El Niño. *Science (1979).* **286**, 2126–2131 (1999).
6. Noh, K. M., Lim, H. G. & Kug, J. S. Global chlorophyll responses to marine heatwaves in satellite ocean color. *Environmental Research Letters* **17**, (2022).
7. Taniguchi, D. A. A., Follows, M. J. & Menden-Deuer, S. Planktonic prey size selection reveals an emergent keystone predator effect and niche partitioning. *PLoS One* **18**, (2023).
8. Berggreen, U., Hansen, B. & Kiorboe, T. *Food Size Spectra, Ingestion and Growth of the Copepod during Development: Implications for Determination of Copepod Production Acartia Tonsa*. *Marine Biology* vol. 99 (1988).

9. Oh, J. W., Pushparaj, S. S. C., Muthu, M. & Gopal, J. Review of Harmful Algal Blooms (HABs) Causing Marine Fish Kills: Toxicity and Mitigation. *Plants* vol. 12 Preprint at https://doi.org/10.3390/plants12233936 (2023).
10. Beaugrand, G., Edwards, M. & Legendre, L. Marine biodiversity, ecosystem functioning, and carbon cycles. *Proc. Natl. Acad. Sci. U. S. A.* **107**, 10120–10124 (2010).
11. Bracher, A. *et al.* Obtaining phytoplankton diversity from ocean color: A scientific roadmap for future development. *Frontiers in Marine Science* vol. 4 Preprint at https://doi.org/10.3389/fmars.2017.00055 (2017).
12. Dutkiewicz, S. *et al.* Dimensions of marine phytoplankton diversity. *Biogeosciences* **17**, 609–634 (2020).
13. Henson, S. A., Cael, B. B., Allen, S. R. & Dutkiewicz, S. Future phytoplankton diversity in a changing climate. *Nat. Commun.* **12**, 1–8 (2021).
14. Cael, B. B., Dutkiewicz, S. & Henson, S. Abrupt shifts in 21st-century plankton communities. *Sci. Adv.* **7**, 1–10 (2021).
15. Acevedo-Trejos, E., Brandt, G., Bruggeman, J. & Merico, A. Mechanisms shaping size structure and functional diversity of phytoplankton communities in the ocean. *Sci. Rep.* **5**, (2015).
16. Arteaga, L. A. & Rousseaux, C. S. Impact of Pacific Ocean heatwaves on phytoplankton community composition. *Commun. Biol.* **6**, (2023).
17. Benedetti, F. *et al.* Major restructuring of marine plankton assemblages under global warming. *Nat. Commun.* **12**, 1–15 (2021).
18. Acevedo-Trejos, E. *et al.* Modelling approaches for capturing plankton diversity (MODIV), their societal applications and data needs. *Front. Mar. Sci.* **9**, 1–9 (2022).
19. Hobday, A. J. *et al.* A hierarchical approach to defining marine heatwaves. *Prog. Oceanogr.* **141**, 227–238 (2016).
20. McCabe, R. M. *et al.* An unprecedented coastwide toxic algal bloom linked to anomalous ocean conditions. *Geophys. Res. Lett.* **43**, 10,366-10,376 (2016).
21. Brown, M. V. *et al.* A marine heatwave drives significant shifts in pelagic microbiology. *Commun. Biol.* **7**, 1–14 (2024).
22. Qiu, Z., Qiao, F., Jang, C. J., Zhang, L. & Song, Z. Evaluation and projection of global marine heatwaves based on CMIP6 models. *Deep. Sea. Res. 2. Top. Stud. Oceanogr.* **194**, (2021).
23. Frölicher, T. L., Fischer, E. M. & Gruber, N. Marine heatwaves under global warming. *Nature* **560**, 360–364 (2018).
24. Oliver, E. C. J. *et al.* Projected marine heatwaves in the 21st century and the potential for ecological impact. *Front. Mar. Sci.* **6**, 734 (2019).
25. Lee, C., Song, H., Choi, Y., Cho, A. & Marshall, J. Observed multi-decadal increase in the surface ocean's thermal inertia. *Nat. Clim. Chang.* **15**, 308–314 (2025).
26. Aumont, O., Ethé, C., Tagliabue, A., Bopp, L. & Gehlen, M. PISCES-v2: An ocean biogeochemical model for carbon and ecosystem studies. *Geosci. Model Dev.* **8**, 2465–2513 (2015).
27. Stock, C. A., Dunne, J. P. & John, J. G. Global-scale carbon and energy flows through the marine planktonic food web: An analysis with a coupled physical-biological model. *Prog. Oceanogr.* **120**, 1–28 (2014).

28. Dunne, J. P., Gnanadesikan, A., Sarmiento, J. L. & Slater, R. D. *Technical Description of the Prototype Version (v0) of Tracers Of Phytoplankton with Allometric Zooplankton (TOPAZ) Ocean Biogeochemical Model as Used in the Princeton IFMIP * Model †*. (2010).

29. Eppley, R. W. Temperature and phytoplankton growth in the sea. *Fishery Bulletin* **70**, (1972).

30. Sathyendranath, S. *et al.* An ocean-colour time series for use in climate studies: the experience of the ocean-colour climate change initiative (OC-CCI). *Sensors* **19**, 4285 (2019).

31. Sathyendranath, S. *et al.* Monthly climatology of global ocean colour data products at 4km resolution, Version 6.0. *NERC EDS Centre for Environmental Data Analysis*.

32. Huang, B. *et al.* Improvements of the daily optimum interpolation sea surface temperature (DOISST) version 2.1. *J. Clim.* **34**, 2923–2939 (2021).

33. Oliver, E. C. J. *et al.* Longer and more frequent marine heatwaves over the past century. *Nat. Commun.* **9**, 1–12 (2018).

34. Hayashida, H., Matear, R. J., Strutton, P. G. & Zhang, X. Insights into projected changes in marine heatwaves from a high-resolution ocean circulation model. *Nat. Commun.* **11**, (2020).

35. Sen Gupta, A. *et al.* Drivers and impacts of the most extreme marine heatwaves events. *Sci. Rep.* **10**, 1–15 (2020).

36. Doney, S. C. Plankton in a warmer world. *Nature* **444**, 695–696 (2006).

37. Lévy, M., Jahn, O., Dutkiewicz, S. & Follows, M. J. Phytoplankton diversity and community structure affected by oceanic dispersal and mesoscale turbulence. *Limnology and Oceanography: Fluids and Environments* **4**, 67–84 (2014).

38. Clayton, S., Dutkiewicz, S., Jahn, O. & Follows, M. J. Dispersal, eddies, and the diversity of marine phytoplankton. *Limnology and Oceanography: Fluids and Environments* **3**, 182–197 (2013).

39. Soininen, J., Passy, S. & Hillebrand, H. The relationship between species richness and evenness: A meta-analysis of studies across aquatic ecosystems. *Oecologia* **169**, 803–809 (2012).

40. Mackey, D. J., Blanchot, J., Higgins, H. W. & Neveux, J. *Phytoplankton Abundances and Community Structure in the Equatorial Pacific*. *Deep-Sea Research II* vol. 49 (2002).

41. Stukel, M. R., Landry, M. R. & Selph, K. E. Nanoplankton mixotrophy in the eastern equatorial Pacific. *Deep. Sea. Res. 2. Top. Stud. Oceanogr.* **58**, 378–386 (2011).

42. Matsumoto, K., Furuya, K. & Kawano, T. Association of picophytoplankton distribution with ENSO events in the equatorial Pacific between 145°E and 160°W. *Deep. Sea. Res. 1. Oceanogr. Res. Pap.* **51**, 1851–1871 (2004).

43. Edwards, K. F., Thomas, M. K., Klausmeier, C. A. & Litchman, E. Allometric scaling and taxonomic variation in nutrient utilization traits and maximum growth rate of phytoplankton. *Limnol. Oceanogr.* **57**, 554–566 (2012).

44. Branco, P., Egas, M., Hall, S. R. & Huisman, J. Why do phytoplankton evolve large size in response to grazing? *American Naturalist* **195**, E20–E37 (2020).

45. Leibold, M. A. *et al.* The metacommunity concept: A framework for multi-scale community ecology. *Ecology Letters* vol. 7 601–613 Preprint at https://doi.org/10.1111/j.1461-0248.2004.00608.x (2004).

46. Armstrong, R. A. *Stable Model Structures for Representing Biogeochemical Diversity and Size Spectra in Plankton Communities*.

47. Bray, J. R. & Curtis, J. T. An ordination of the upland forest communities of southern Wisconsin. *Ecol. Monogr.* **27**, 326–349 (1957).

48. Devictor, V., Julliard, R., Couvet, D. & Jiguet, F. Birds are tracking climate warming, but not fast enough. *Proceedings of the Royal Society B: Biological Sciences* **275**, 2743–2748 (2008).

49. Bjerknes, J. Atmospheric teleconnections from the equatorial Pacific. *Mon. Weather Rev.* **97**, 163–172 (1969).

50. Barber, R. T. & Chavez, F. P. Biological Consequences of El Niño. *Science (1979).* **222**, 1203–1210 (1983).

51. Park, J. Y., Kug, J. S., Bader, J., Rolph, R. & Kwon, M. Amplified Arctic warming by phytoplankton under greenhouse warming. *Proc. Natl. Acad. Sci. U. S. A.* **112**, 5921–5926 (2015).

52. Meskhidze, N. & Nenes, A. *Phytoplankton and Cloudiness in the Southern Ocean*. https://www.science.org.

53. Vallina, S. M. *et al.* Global relationship between phytoplankton diversity and productivity in the ocean. *Nat. Commun.* **5**, (2014).

54. Sommer, U., Charalampous, E., Genitsaris, S. & Moustaka-Gouni, M. Benefits, costs and taxonomic distribution of marine phytoplankton body size. *Journal of Plankton Research* vol. 39 494–508 Preprint at https://doi.org/10.1093/plankt/fbw071 (2017).

55. Serra-Pompei, C. *et al.* Linking Plankton Size Spectra and Community Composition to Carbon Export and Its Efficiency. *Global Biogeochem. Cycles* **36**, (2022).

56. Marshall, J., Adcroft, A., Hill, C., Perelman, L. & Heisey, C. A finite-volume, incompressible navier stokes model for, studies of the ocean on parallel computers. *J. Geophys. Res. Oceans* **102**, 5753–5766 (1997).

57. Zhang, H., Menemenlis, D. & Fenty, I. *ECCO LLC270 Ocean-Ice State Estimate*. (2018).

58. NASA. *Estimating the Circulation & Climate of the Ocean (ECCO) Product Accessed via NASA Data Portal*. https://data.nas.nasa.gov/ecco/llc_270/iter42/input/.

59. ECCO Consortium *et al. Synopsis of the ECCO Central Production Global Ocean and Sea-Ice State Estimate, Version 4 Release 4 (4 Release 4). Zenodo.* (2021) doi:https://doi.org/10.5281/zenodo.4533349.

60. Adcroft, A. *et al. Darwin Project*. https://github.com/darwinproject/darwin3/.

61. Dutkiewicz, S. *et al.* Capturing optically important constituents and properties in a marine biogeochemical and ecosystem model. *Biogeosciences* **12**, 4447–4481 (2015).

62. Gregg, W. W. & Casey, N. W. Skill assessment of a spectral ocean-atmosphere radiative model. *Journal of Marine Systems* **76**, 49–63 (2009).

63. Pilo, G. S., Holbrook, N. J., Kiss, A. E. & Hogg, A. M. C. Sensitivity of Marine Heatwave Metrics to Ocean Model Resolution. *Geophys. Res. Lett.* **46**, 14604–14612 (2019).

64. Hayashida, H., Matear, R. J., Strutton, P. G. & Zhang, X. Insights into projected changes in marine heatwaves from a high-resolution ocean circulation model. *Nat. Commun.* **11**, (2020).

65. Chassignet, E. P. *et al.* Impact of horizontal resolution on global ocean-sea ice model simulations based on the experimental protocols of the Ocean Model Intercomparison Project phase 2 (OMIP-2). *Geosci. Model Dev.* **13**, 4595–4637 (2020).

66. Pielou, E. C. The measurement of diversity in different types of biological collections. *J. Theor. Biol.* **13**, 131–144 (1966).

641 67. Kim, H. *et al*. Dataset for 'Marine Heatwaves Disrupt Phytoplankton Communities Through
642 Trait-Dependent Selection'. doi:10.6084/m9.figshare.32346735.

643

644 Supporting Information for

645

646

647 Marine Heatwaves Disrupt Phytoplankton 648 Communities Through Trait-dependent Selection

649

650

651 Kim et al.

652 Corresponding author: Hajoon Song, hajsong@yonsei.ac.kr

653

654 This PDF file includes:

655 Table S1

656 Figs. S1 to S10

657

658

	PFT	Climatology	MHW		
			Mean	5th percentile	95th percentile
Equatorial Pacific	*Prochlorococcus*	1.474	1.596	1.600	1.639
	Synechococcus	1.996	1.811	1.818	1.848
	Picoeukaryote	4.016	3.749	3.759	3.830
	Haptophyte	8.641	5.997	6.113	6.268
	Diazotroph	0.007	0.001	0.001	0.001
	Trichodesmium	0.049	0.010	0.009	0.012
	Diatom	6.168	3.001	3.078	3.201
	Dinoflagellate	16.075	10.430	10.608	10.911
Indian Ocean	*Prochlorococcus*	0.901	1.016	1.013	1.020
	Synechococcus	1.049	1.140	1.131	1.157
	Picoeukaryote	2.182	2.290	2.279	2.313
	Haptophyte	3.903	3.319	3.302	3.349
	Diazotroph	0.868	0.862	0.856	0.881
	Trichodesmium	1.005	0.715	0.705	0.744
	Diatom	1.627	1.236	1.235	1.253
	Dinoflagellate	8.432	6.209	6.082	6.399

Table S1. Mean Richness by PFT for the climatology and MHW periods. The mean richness under climatological and MHW conditions were first calculated at each grid point and then averaged over the corresponding domain. For the MHW periods, 90% bootstrap intervals are also provided (N=5,000). *Trichodesimium* is a nitrogen-fixing type, with a larger size than other diazotrophs. In the main text, it is included within the diazotroph group.

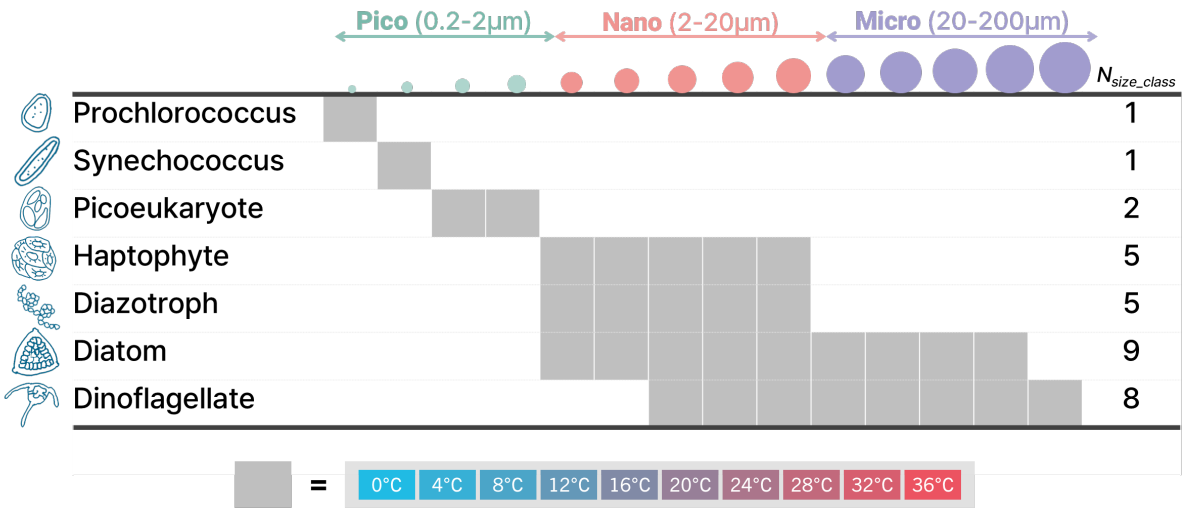

Fig. S1. Phytoplankton types resolved by Darwin in this study. Gray cells indicate the size classes included for each phytoplankton functional type (PFT). The number of size classes for each PFT is shown in the rightmost column, with their total being 31. Each PFT–size combination is further expanded into ten temperature preferences, as illustrated at the bottom of the table and Fig. S2a.

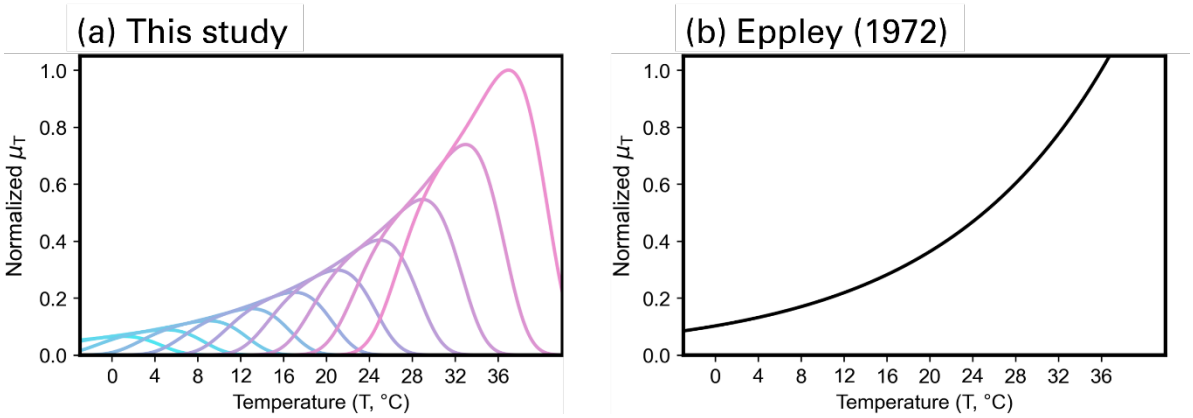

673

674 **Fig. S2. Temperature-dependent phytoplankton growth rate (μ_T). a** Colors represent μ_T
675 curves for different phytoplankton thermal types in the model. Tick marks on the *x*-axis
676 correspond to the optimal temperature values used in this study (0, 4, 8, …, 36 °C). **b** The Eppley
677 curve where μ_T increases monotonically with temperature, used in most models (e.g., ref 26-29).
678 Vertical axes are shown as normalized values with respect to μ_T(T=36 °C) of the 36 °C-preferring
679 type in panel **a** (rightmost pink line), and μ_T(T=36 °C) in panel **b**.

680

681

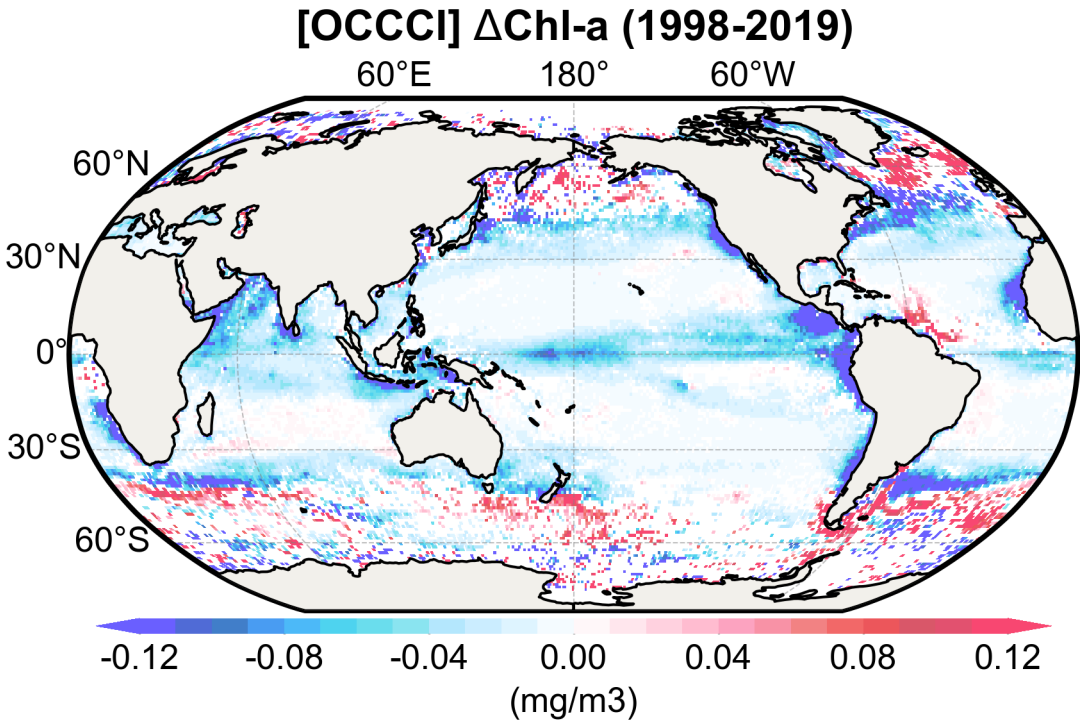

682

683 **Fig. S3. Satellite-derived chlorophyll-*a* anomalies (mg m^{-3}) averaged during MHW periods**
684 **(1998–2019).** Data were obtained from the OC-CCI. Only statistically significant results at the
685 95% confidence level are displayed based on Student's *t*-test.

686

687

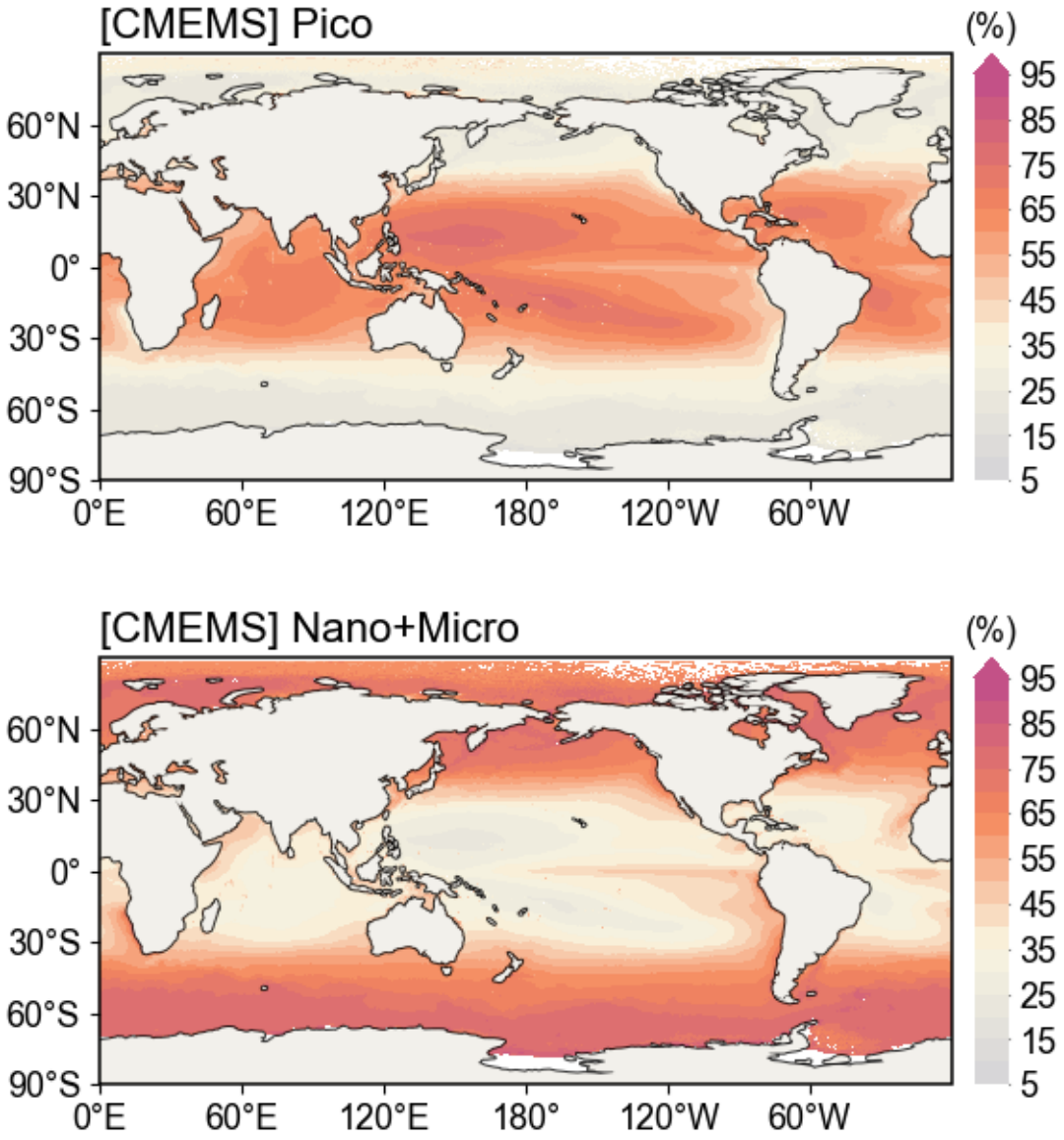

Fig. S4. Satellite-derived mean percentage (%) of each phytoplankton size class (2003–2024). Top: picophytoplankton (diameter < 2 µm). **Bottom**: combined nano- and micro-phytoplankton (diameter > 2 µm). Data were obtained from the Copernicus-GlobColour repository68,69.

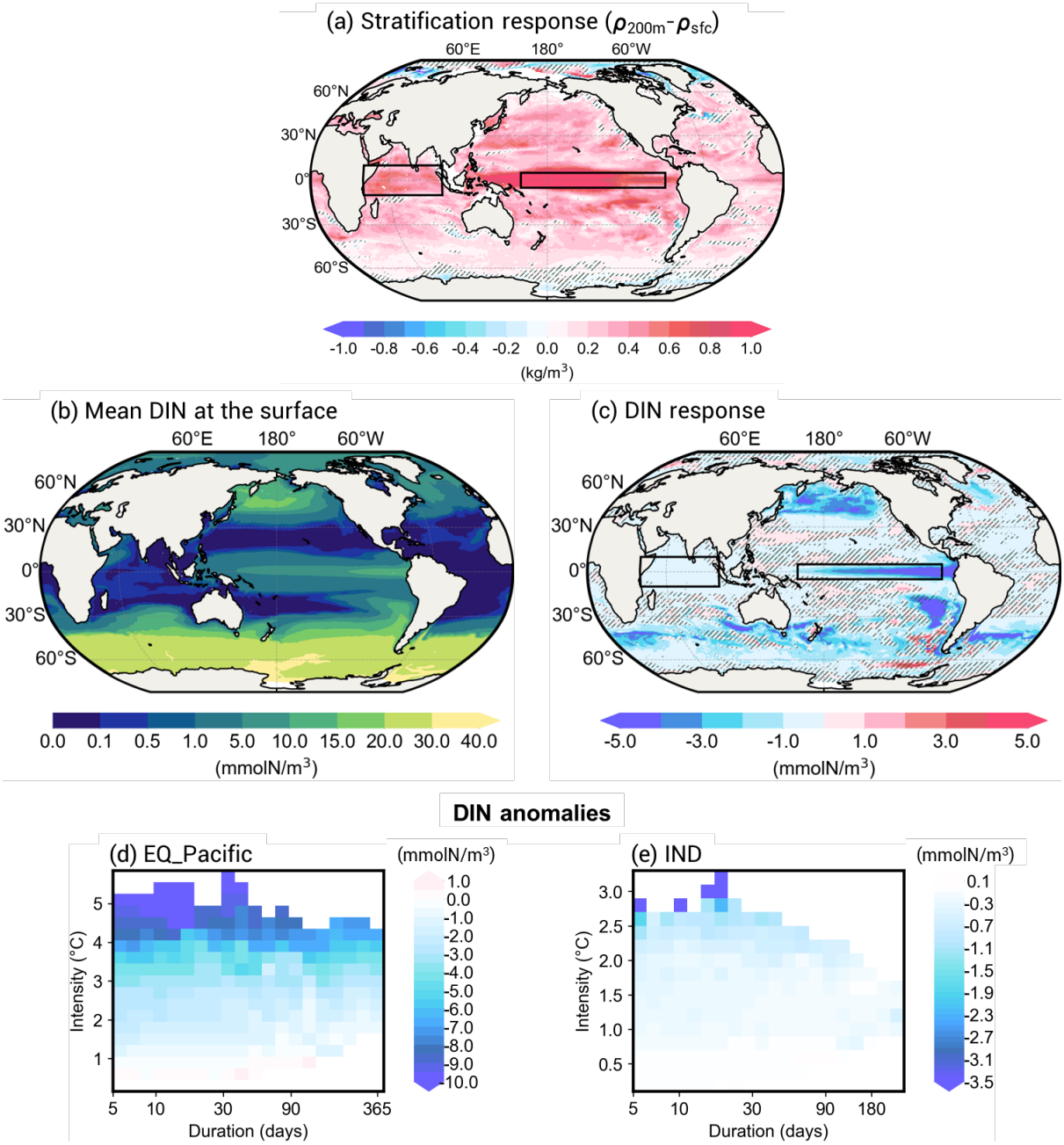

Fig. S5. Stratification and surface dissolved inorganic nitrogen (DIN). a Anomalies of vertical gradient of seawater density ($\rho_{200m}-\rho_{sfc}$, an indicator of stratification) averaged over MHW periods. **b-c** Climatological mean pattern of DIN and anomalies averaged over MHW periods (in mmol N m^{-3}). **d-e** Anomalies of DIN concentrations as a function of MHW intensity and duration.

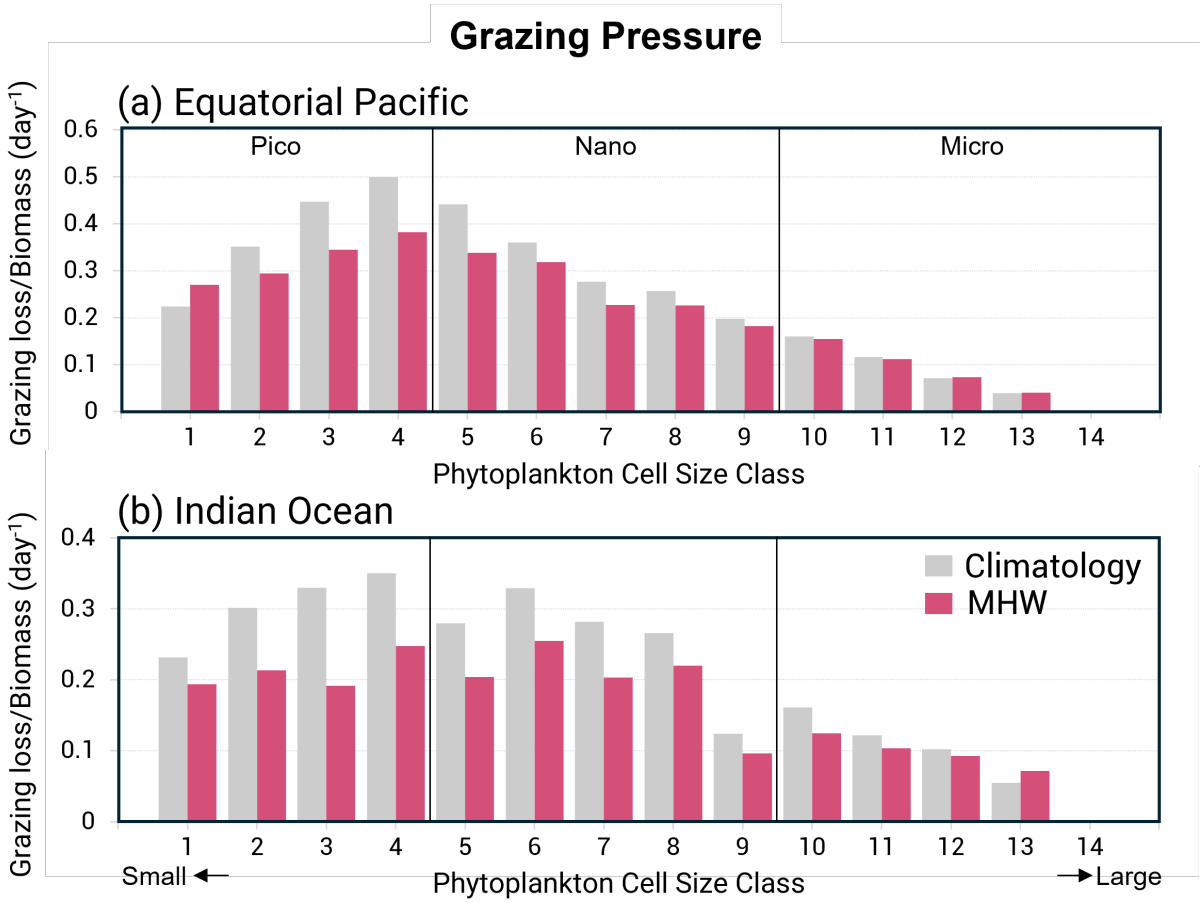

Fig. S6. Grazing pressure for each phytoplankton cell size class. Grazing pressure for each size class, measured as the ratio of grazing loss (mmolC m^{-3} day^{-1}) to biomass (mmolC m^{-3}). The cell size classes correspond to the columns in Fig. S1. Grey and red represent climatological and MHW periods, respectively. **a** for the equatorial Pacific and **b** for the Indian Ocean.

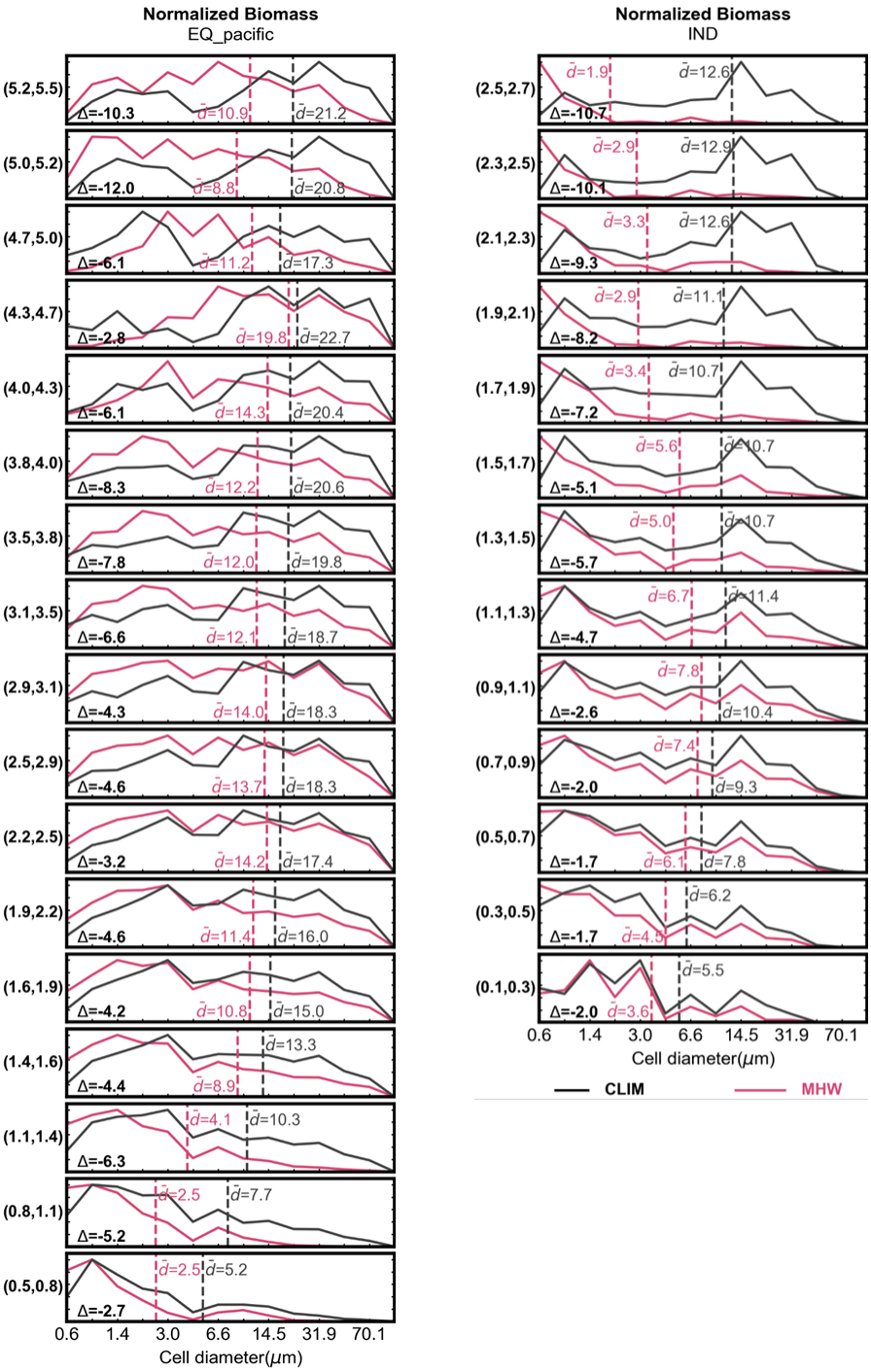

Fig. S7. Phytoplankton size distributions under different heatwaves intensities. Phytoplankton size distributions are shown for different heatwave intensity ranges. Heatwaves with durations of 12–15 days in the equatorial Pacific and 11–14 days in the Indian Ocean are considered. These duration bins were selected as representative examples (dashed lines in Fig. 3c,g). In each panel, the heatwave intensity range is indicated in parentheses on the left: (I_1, I_2) denotes heatwaves with intensities between I_1 and I_2. On the *y*-axis, biomass is normalized by the maximum value so that it ranges between 0 and 1. Black represents climatological conditions over grid points that experienced at least one heatwave with the corresponding intensity and duration, whereas pink represents MHW conditions. The community-mean diameter ($\bar{d}$) is denoted by dashed vertical lines. The difference between MHW and non-MHW conditions (Δ)

722 is shown in the lower-left corner, which is identical to the values shown in colors in Fig. 3c,g.
723 The *x*-axis is shown on a logarithmic scale.

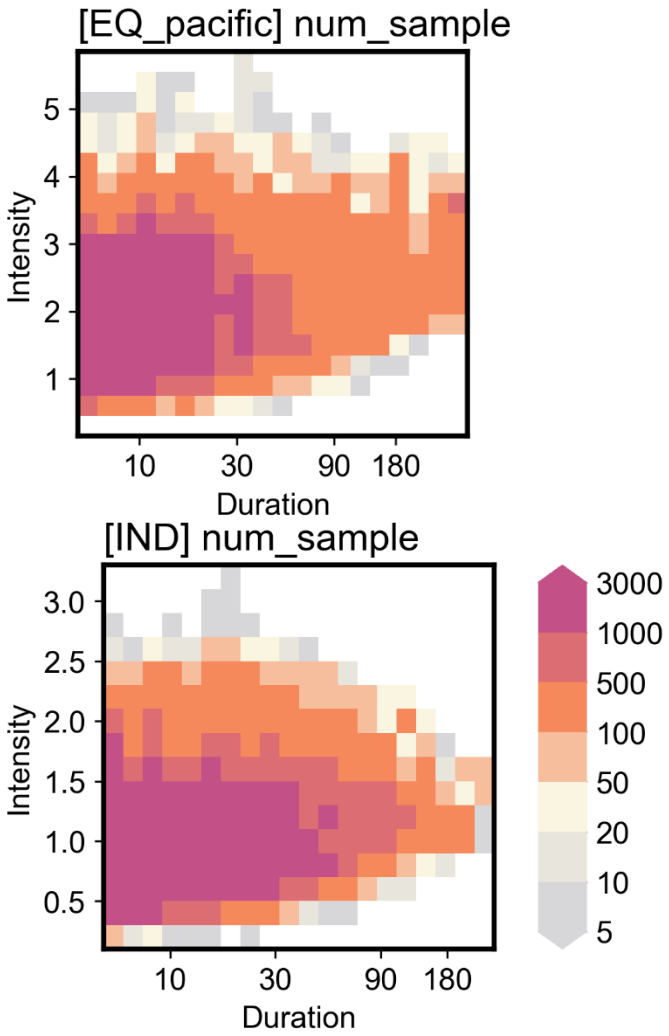

Fig. S8. Number of heatwave events as a function of MHW intensity and duration. The color bar is on an irregular scale.

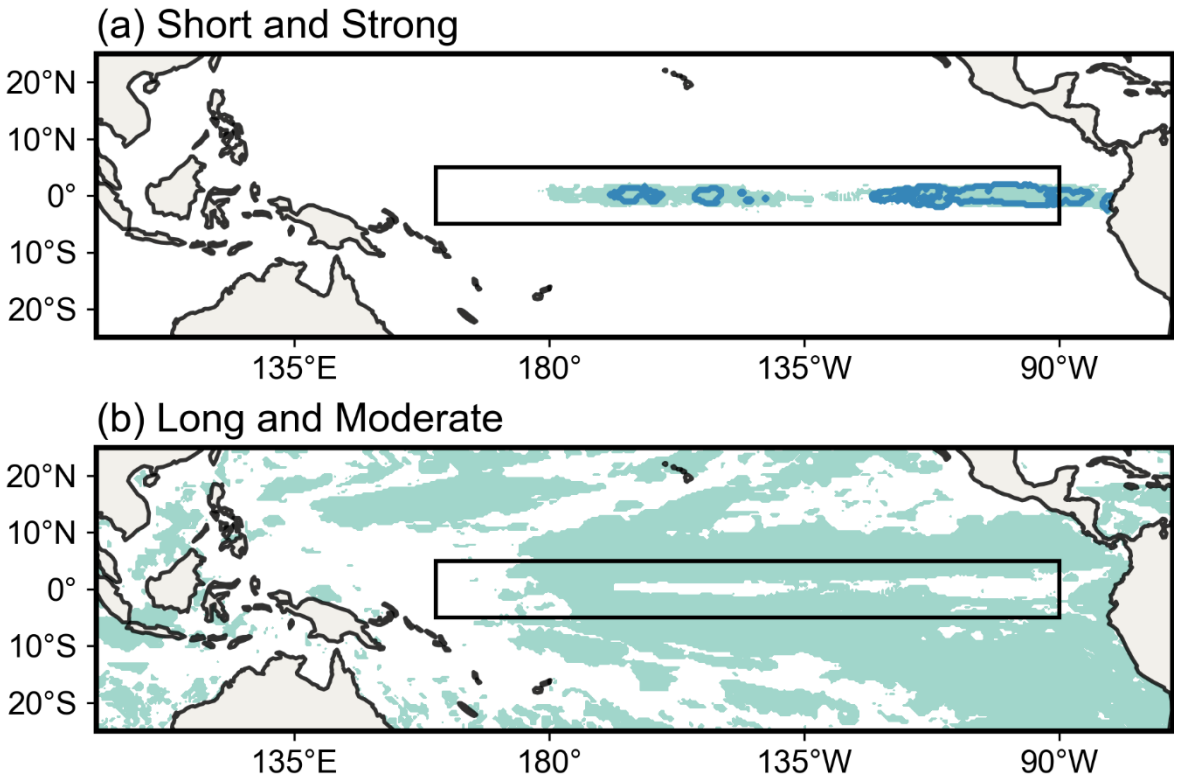

Fig. S9. Regional masks for two heatwave categories. a Grid points at which short and strong heatwaves (intensity ≥ 3.5 °C and duration < 30 days) occurred at least once are shaded. Grid points experiencing stronger intensities (> 4 °C) are highlighted with blue outlines. **b** Same as **a**, but for long and moderate heatwaves (intensity < 3.5 °C and duration > 90 days). Areas outside the black rectangle are not considered in the analysis.

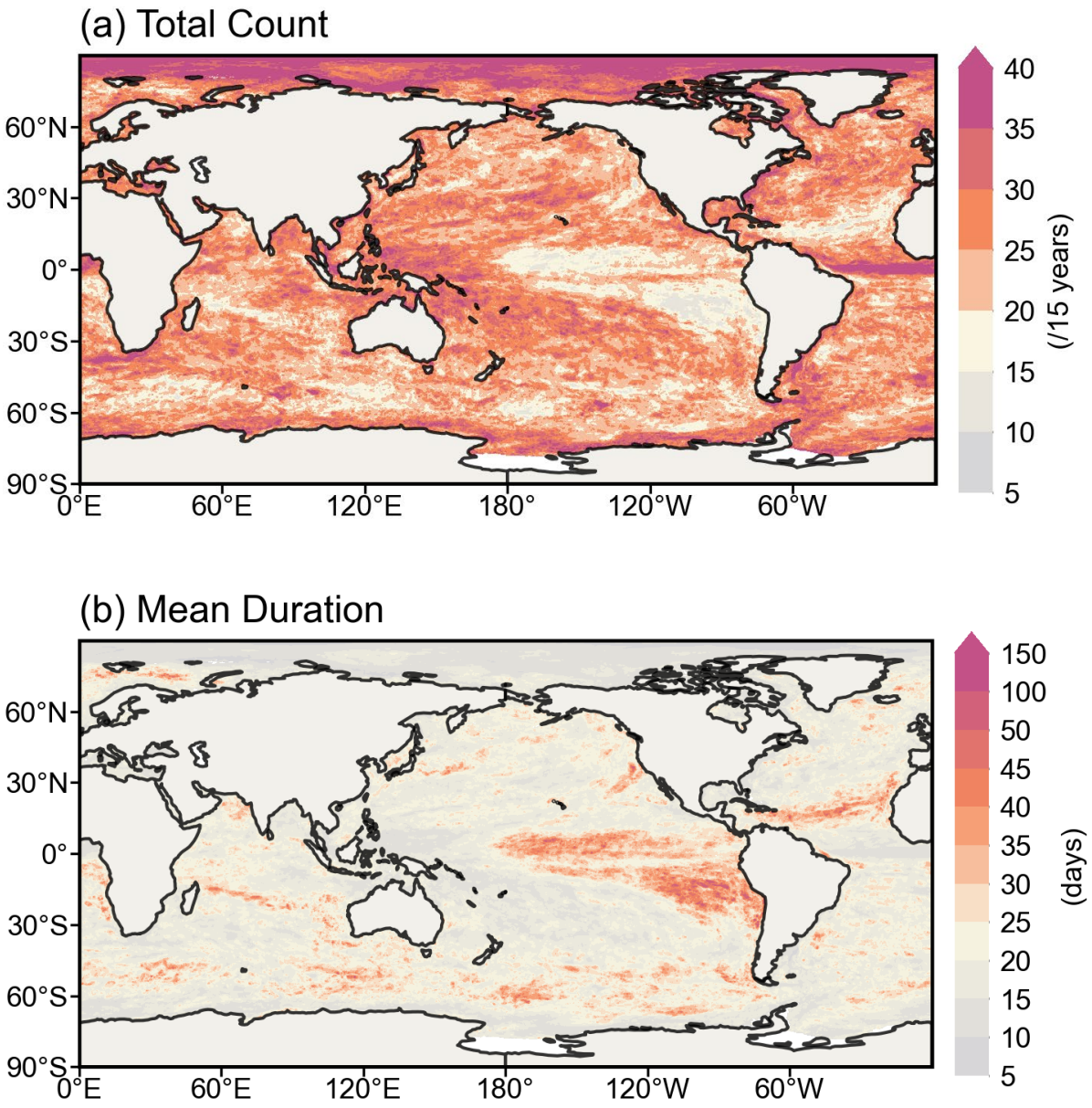

Fig. S10. Simulated patterns of the total number of occurrences and mean duration of heatwaves.

References

68. E.U. Copernicus Marine Service Information (CMEMS). *Global Ocean Colour (Copernicus-GlobColour), Bio-Geo-Chemical, L4 (Monthly and Interpolated) from Satellite Observations (1997-Ongoing)*. doi:https://doi.org/10.48670/moi-00281.

69. Xi, H. *et al.* Global Chlorophyll a Concentrations of Phytoplankton Functional Types With Detailed Uncertainty Assessment Using Multisensor Ocean Color and Sea Surface Temperature Satellite Products. *J. Geophys. Res. Oceans* **126**, (2021).